Chapter 6

Simple hydrothermal route to synthesize $CoO_x(OH)_y/CeO_2/C$ hybrid for enhanced oxygen reduction and evolution reactions

Outline

In the previous chapters, we have explored the oxide-oxide interfaces between spinel cobalt oxide (Co_3O_4) and cubic ceria (CeO_2). From the findings of the previous chapters, we presume that similar interfaces between hydroxide and/or oxyhydroxides of cobalt should also be influenced by CeO_2. Therefore, we proceed to investigate the oxide-hydroxide interfaces between trigonal CoOOH oxyhydroxide (also referred as Heterogenite) and cubic CeO_2. Layered transition-metal oxyhydroxides are an emerging class of mixed metal oxides. In recent times, oxyhydroxides like NiOOH and CoOOH are widely employed as state-of-the-art catalysts in water electrolysers and fuel cells, specifically for alkaline OER. These are cost-effective, easier to synthesize and are more viable for prolonged use [1]. As the entire thesis work is mostly focused on cobalt-based electrocatalysts, we conduct the current study with $CoO_x(OH)_y$ and its CeO_2-modified hybrids. These carbon supported hybrid materials are mentioned as $CoO_x(OH)_y/CeO_2/C$. There already exists numerous reports on the OER mechanism of CoOOH [2]. But fewer reports are available that discusses its ORR aspect. Hence, in this study, we lay more importance in exploring the ORR aspect of $CoO_x(OH)_y$ and $CoO_x(OH)_y/CeO_2$ hybrids. Three variants of $CoO_x(OH)_y/CeO_2/C$ with different atomic ratios of cobalt to cerium (Co:Ce=1:1, 3:1 and 9:1) have been studied against their non-hybrid counterparts $CoO_x(OH)_y/C$ and CeO_2/C toward ORR and OER. This chapter is a comparative study on the effects on varying degree of CeO_2 in $CoO_x(OH)_y$ on its physicochemical properties. Varying CeO_2 content is used as the mediator to engineer electronic configuration in the electroactive $CoO_x(OH)_y$. Detailed physicochemical properties of the catalysts have been presented and correlated with their electrochemical activities. The aim of the study is to understand structure-activity correlation of CeO_2-mediated cobalt oxyhydroxide toward ORR and OER.

The synthesis procedure of the catalysts $CoO_x(OH)_y/C$, CeO_2/C and the three variants of $CoO_x(OH)_y/CeO_2/C$ (shortly denoted as Co/Ce/C-1:1, Co/Ce/C-3:1 and Co/Ce/C-9:1) are described in Section 2.2.10, 2.2.11, 2.2.12, 2.2.13 and 2.2.14 respectively. Their physical characterizations and electrocatalytic activities have been described below.

6.1 Results and discussion

6.1.1 Physical characterization

To characterize the crystallinity of the catalysts, we carried out PXRD measurements and presented them in Figure 6.1.

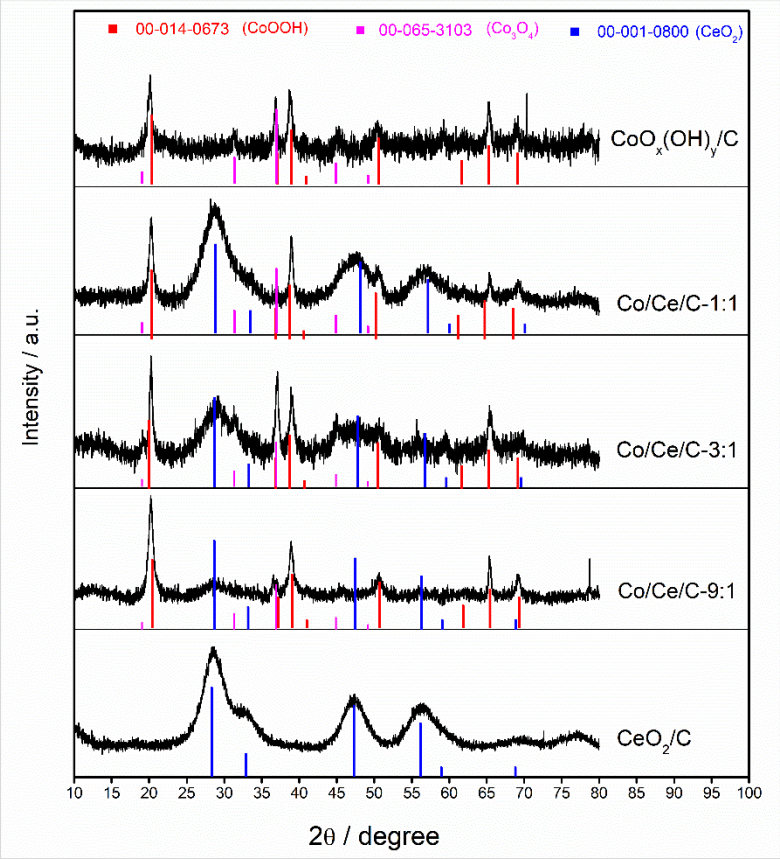

Figure 6.1. PXRD of $CoO_x(OH)_y/C$ and the Co/Ce/C hybrids with JCPDS indexes.

The diffraction peaks occurring at 2θ= 20.2°, 36.9°, 38.8°, 40.8°, 50.5°, 61.7°, 65.3°, 68.2° correspond to (003), (101), (012), (006), (104), (015), (107), (110), (018) and (113) planes respectively, of the trigonal CoOOH (also called Heterogenite, JCPDS #00-014-0673) of space group R-3m [3,4]. There are also some low intense peaks observed at

2θ= 19.0°, 31.3°, 36.9°, 44.9°, 49.2°, 59.5° and 65.4° corresponding to planes (111), (220), (311), (400), (331), (422), (511) and (440) of cubic phase of Co_3O_4 (JCPDS #00-065-3103) [5,6]. It is observed that the peaks for Co_3O_4 phase varies in intensities in the three hybrids Co/Ce/C-1:1, Co/Ce/C-3:1 and Co/Ce/C-9:1. For example, the peak at 2θ=36.9° arising from (311) plane of Co_3O_4 is most pronounced in $CoO_x(OH)_y/C$ and Co/Ce/C-3:1, while for the other catalysts, it is less prominent. The peaks at 2θ= 28.6, 33.2°, 47.8°, 56.7°, 59.6° and 69.5° correspond to (111), (200), (220), (311), (222) and (400) planes respectively, of cubic CeO_2 (JCPDS #00-001-0800) of space group Fm-3m, agreeing with previous reported results [7,8].

FTIR is done to detect presence of functional groups at the surface of the catalysts and is shown in Figure 6.2 (a). The broad band at ~3400 cm^{-1} confirms that the catalysts have surface adsorbed −OH groups [9]. The two sharp and low-intense bands at ~2925 cm^{-1} and ~2825 cm^{-1} are the C−H stretching bonds of the methylene groups (− CH_2−) present in the framework of graphene nanoplatelets. Another low-intense singlet band at ~1565 cm^{-1} arises from the O−H bending mode of adsorbed H_2O molecules [10]. On the fingerprint region of the spectra, the sharp and intense peaks observed at ~654 cm^{-1} and ~574 cm^{-1} arise from Co−O bonds in the $CoO_x(OH)_y/C$ lattice [9,11].

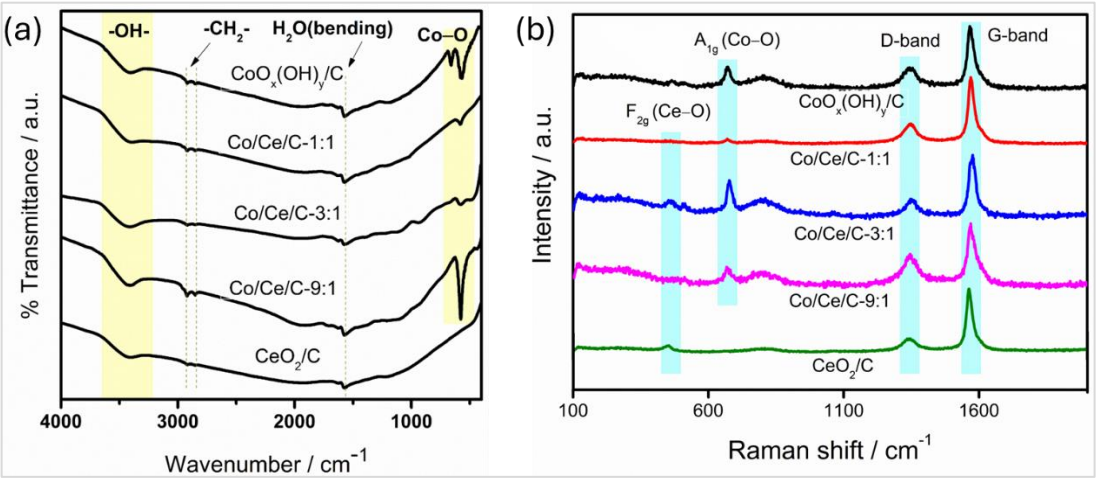

Figure 6.2. (a) FTIR spectra, and (b) Raman spectra of the catalysts with functional groups and vibrational modes indexed.

The presence of some of the vibrational modes of $CoO_x(OH)_y$ and CeO_2 can be confirmed from their Raman spectra, presented in Figure 6.2(b). The Raman peaks observed at ~680 cm^{-1} correspondes too $CoO_x(OH)_y/C$ (A_{1g}) [12,13]. The peak observed at ~460 cm^{-1} arises from F_{2g} mode of CeO_2 [14]. The sharp peaks observed at ~1350 cm^{-1} and 1560 cm^{-1} are typical of graphene nanoplatelets. They signify the D-band (representing sp^3 C) and G-band (sp^2 C) respectively [15,16]. As the catalysts are supported with graphene nanoplatelets in 70 wt%, all of them exhibit the two typical sharp peaks viz. D-band at ~1350 cm^{-1} and G-band at ~1560 cm^{-1}. The D-band represents sp^3 C-atoms and G-band represents sp^2 C-atoms [15,16]. To confirm the elemental composition of Co and Ce in the catalysts, ICP-OES was performed. The results are shown in Table 6.1.

Table 6.1. Atomic ratios of Co and Ce from ICP-OES.

Catalyst	Detectable Co (wt%)	Detectable Ce (wt%)	Co/Ce wt% from ICP-OES	Co/Ce atomic ratio
Co/Ce/C-1:1	17.7	42.3	0.41	1:1
Co/Ce/C-3:1	36.6	28.9	1.26	3:1
Co/Ce/C-9:1	50.5	12.0	4.19	9:1

The structure and morphology of the materials are studied by TEM imaging. Figure 6.3 presents the TEM images of $CoO_x(OH)_y/C$ and the hybrids $CoO_x(OH)_y/CeO_2/C$ (1:1, 3:1 and 9:1). It is observed that $CoO_x(OH)_y/C$ has two-dimensional hexagonal plate-like structures while the three hybrid materials $CoO_x(OH)_y/CeO_2/C$ (1:1, 3:1 and 9:1) does not exhibit this feature. Instead, these are mostly smaller, lobular and dense.

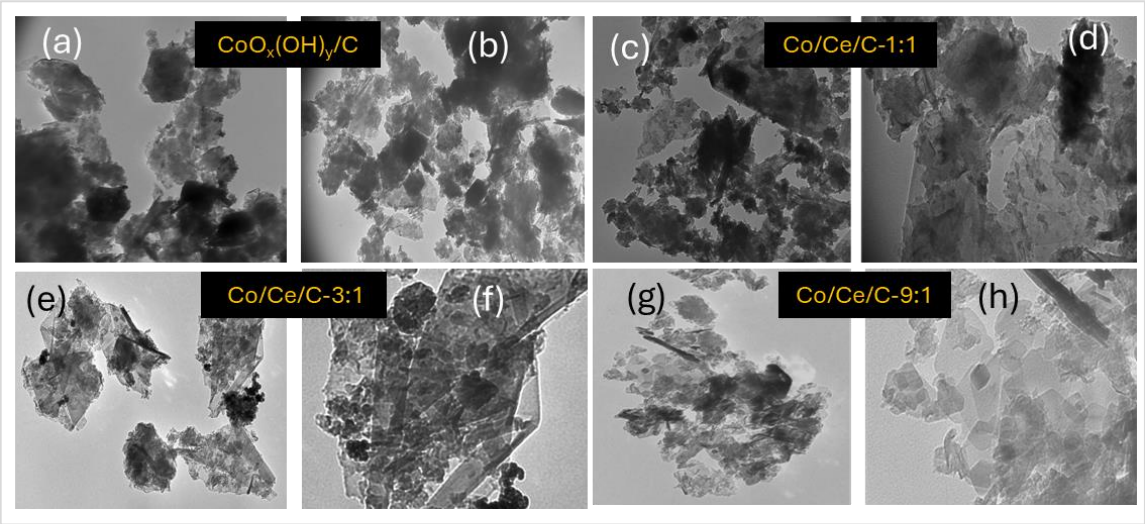

Figure 6.3. TEM images of $CoO_x(OH)_y/C$ and the $CoO_x(OH)_y/CeO_2/C$ (1:1, 3:1 and 9:1) hybrids.

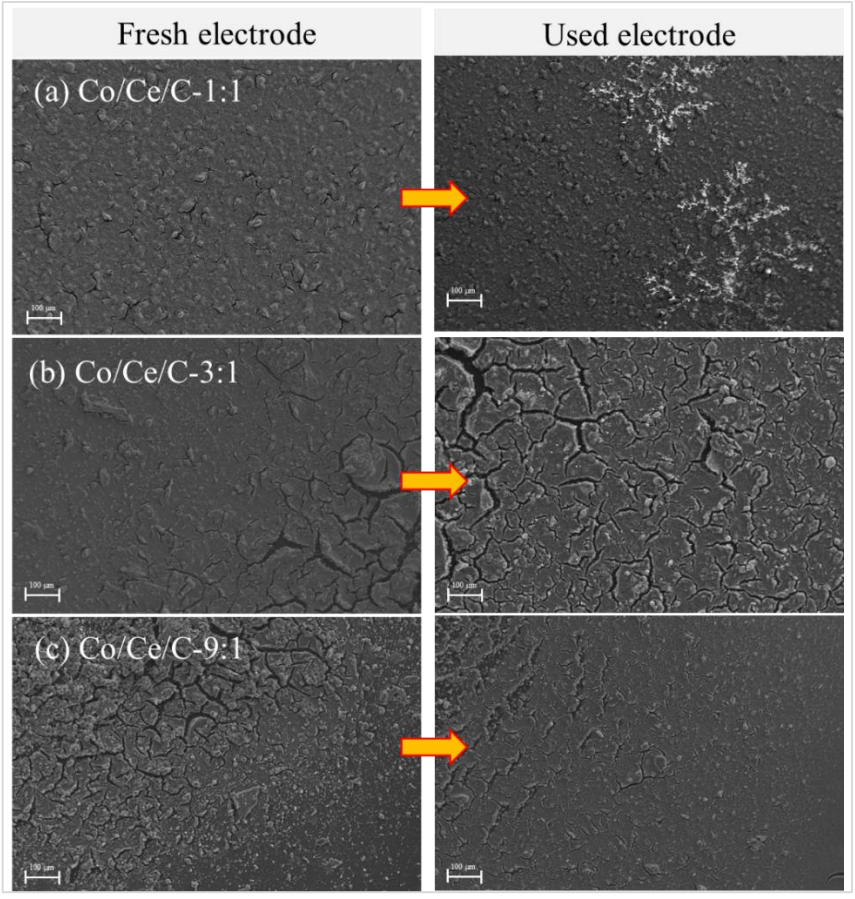

Figure 6.4. FESEM images of freshly drop-casted electrodes and used electrodes of (a) Co/Ce/C-1:1, (b) Co/Ce/C-3:1 and (c) Co/Ce/C-9:1.

To know more about the external morphology, the $CoO_x(OH)_y/CeO_2$ catalysts we have captured the FESEM images of freshly fabricated working electrodes. The same electrodes were again imaged after one potential round of ORR study (consisting of three slow scan CVs and RDE-LSVs) to see any observable structural changes. The images of both fresh and used electrodes are shown in Figure 6.4. The fresh electrodes display nearly smooth surfaces with minimal cracks. The used electrode of Co/Ce/C-1:1 display flower-like oxidized areas while Co/Ce/C-3:1 and Co/Ce/C-9:1 do not display prominent changes after ORR except a few cracks.

The surface elemental composition of the Co/Ce/C hybrids are detected through XPS. Their wide survey spectrum are shown in Figure 6.4. All peaks have been calibrated according to 284.6 eV for adventitious C 1s.

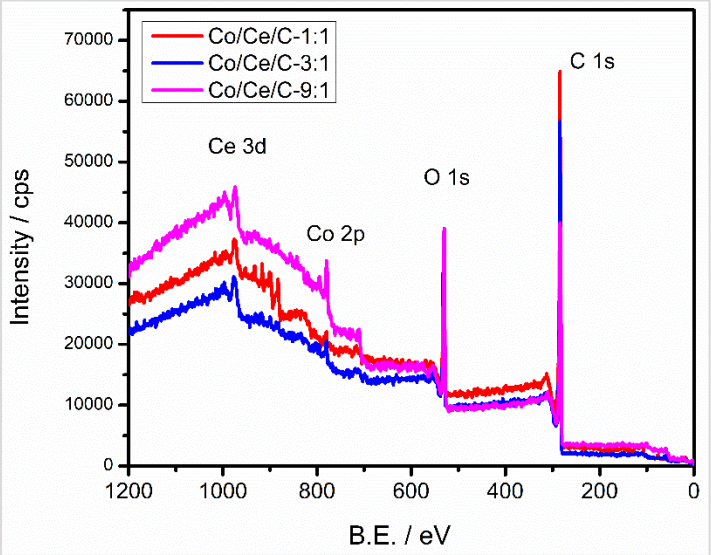

Figure 6.5. XPS survey spectrum of the Co/Ce/C hybrids.

The core XP spectra for Co 2p, Ce 3d and O 1s are deconvoluted. In Figure 6.6 (a), the Co 2p spectra is deconvoluted into two doublets, one for Co $2p_{3/2}$ in the range 792−800 eV and the other for Co $2p_{1/2}$ in the range 783−785 eV, agreeing with other reports [17]. The presence of both Co^{2+} and Co^{3+} is detected for Co/Ce/C-1:1 and Co/Ce/C-3:1 indicating possible presence of Co_3O_4. This is not observed for Co/Ce/C-9:1 which indicates that this ratio of the ions generates pure phase of CoOOH which is concordant with the PXRD peaks observed in Figure 6.1. The binding energies (B.E.) are seen to be

shifting towards lower energy in the hybrids Co/Ce/C-3:1 and Co/Ce/C-9:1. This could be a consequence of the increased ratio of Co^{2+} /Co^{3+}. Figure 6.6 (d) presents the concentration and relative ratio of Co^{2+} and Co^{3+} ions in the Co/Ce/C hybrids derived from area integration method. It is seen that Co^{2+} : Co^{3+} is the highest for $CoO_x(OH)_y/CeO_2$/C 3:1. The peak positions and shifts in Co 2p XP spectra are presented in Table 6.2.

Table 6.2. Peak positions of Co 2p XP spectra in different catalysts and their shifts with respect to one another.

Catalysts	**Co $2p_{3/2}$**				**Co $2p_{1/2}$**			
	Co^{2+}	**Shift / eV**	**Co^{3+}**	**Shift / eV**	**Co^{2+}**	**Shift / eV**	**Co^{3+}**	**Shift / eV**
Co/Ce/C-1:1	797.5		795.8		782.1		780.5	
Co/Ce/C-3:1	796.2	–1.3	794.6	–1.2	781.6	–0.5	780.1	–0.4
Co/Ce/C-9:1	−		795.1	–0.7	−		780.0	–0.5

The Ce 3d core XP spectra for the Co/Ce/C hybrids are presented in Figure 6.6 (b). The spectra exhibit two doublets- around 875−895 eV for Ce $3d_{5/2}$ spin state and around to 895−920 eV for Ce $3d_{3/2}$ spin state. The spectrum is deconvoluted into eight peaks. The assignment of the deconvoluted peaks, relative shifts in binding energies and area integration ratios for Ce 3d XP spectra are presented in Table 6.3. The peak positions are in agreement with other reported literature [9,18]. Similar to the ratio of cobalt ions, the ratio of Ce^{3+} : Ce^{4+} is the highest for $CoO_x(OH)_y/CeO_2$/C 3:1. While the spectra for $CoO_x(OH)_y/CeO_2$ with Co/Ce/C-1:1 and Co/Ce/C-3:1 could be deconvoluted into 8 distinct peaks, the one for Co/Ce/C- 9:1 is not differentiable due to minimal quantity of CeO_2 in it.

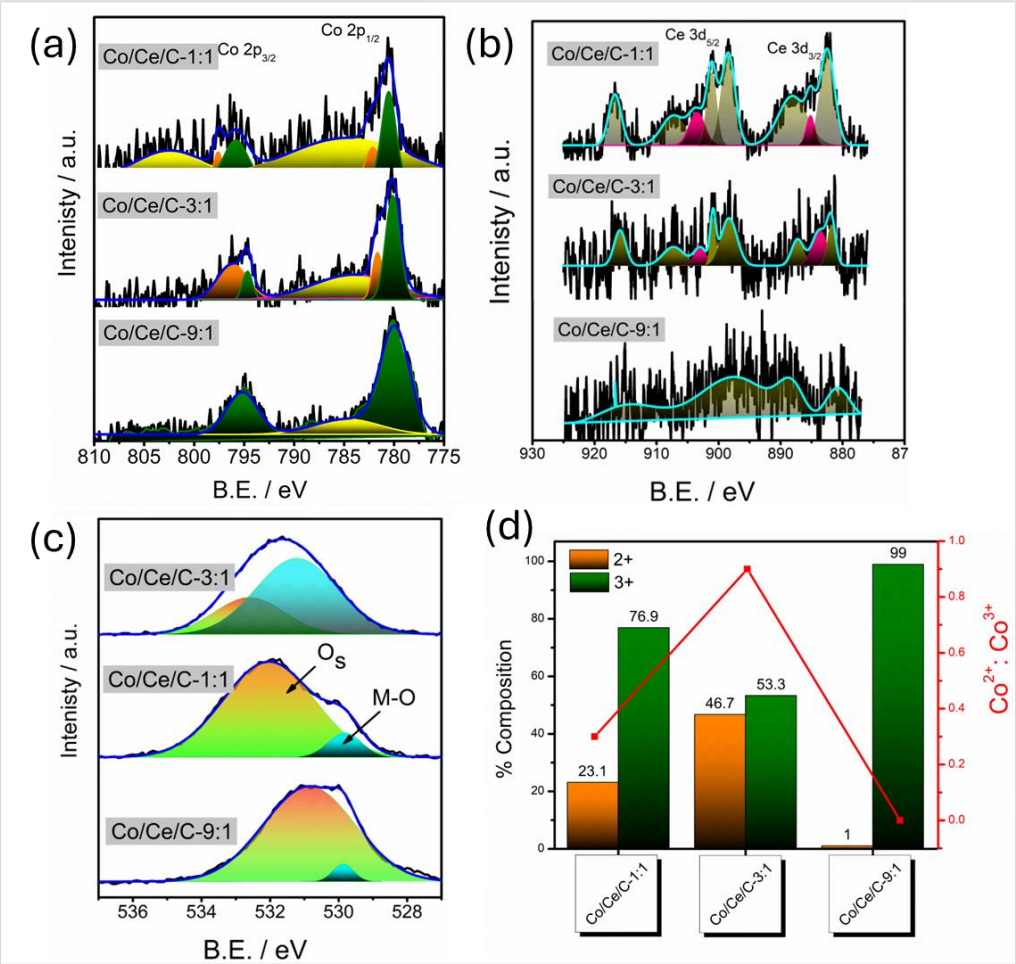

Figure 6.6. Core XP spectra of the Co/Ce/C hybrids for (a) Co 2p, (b) Ce 3d, (c) O 1s and (d) Bar diagram representing %composition of $Co^{2+/3+}$ ions and Co^{2+}/Co^{3+} ratio.

These two observations indicate that the hybrid Co/Ce/C-3:1 has the greatest number of point defects in its lattice.

Similarly, the O 1s core XP spectra is also deconvoluted into two component peaks in the range 536−528 eV. The lower energy component occurring at ~530 eV represents the lattice oxygen (M− O, M=Co, Ce) and one at slightly higher energy at ~532 eV represents surface oxygen (physisorbed and chemisorbed M− OH, M=Co, Ce). These values are in good agreement with previously reported literature [9,19,20]. As there are multiple metal-oxygen bonds in the $CoO_x(OH)_y/CeO_2$, the quantification of oxygen vacancies is not estimated from area integration method. Instead, we perform EPR at room temperature to compare the spin states and oxygen vacancies in them. The spin state of

transition metal oxides and hydroxides is strongly correlated with their catalytic activities [21].

Table 6.3. Peak positions and area integration ratios of Ce 3d XP spectra.

Doublet	Species	Peak position / eV		Shift / eV	Ce^{3+} : Ce^{4+}	
		$CoO_x(OH)_y/CeO_2/C$			$CoO_x(OH)_y/CeO_2/C$	
		1:1	3:1		1:1	3:1
Ce $3d_{5/2}$	Ce^{3+}	885.1	883.5	-1.6	0.12	0.30
	Ce^{4+}	882.3	881.7	-0.6		
		888.1	887.2	-0.9		
		898.4	898.2	-0.2		
		901.2	900.7	-0.5		
Ce $3d_{3/2}$	Ce^{3+}	903.7	903.0	-0.7		
	Ce^{4+}	907.4	907.2	-0.2		
		916.7	915.8	-0.9		

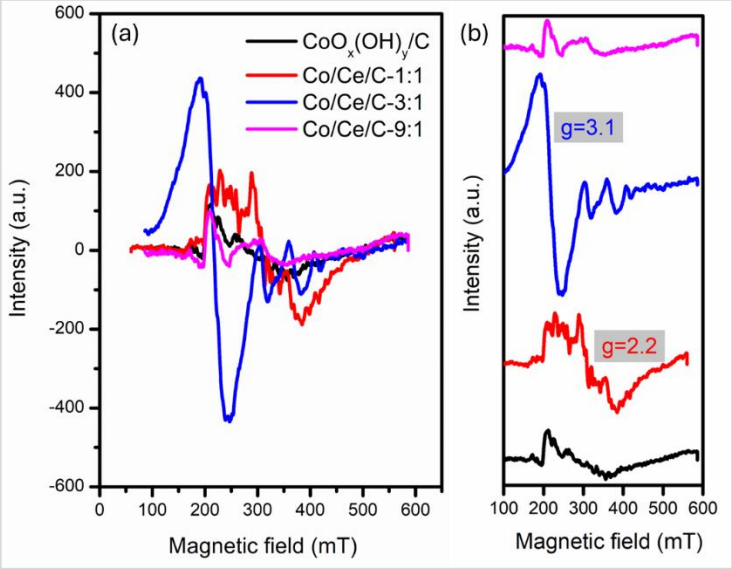

Figure 6.7. EPR spectra of $CoO_x(OH)_y/C$ and Co/Ce/C hybrids (a) overlay view for intensity comparison, and (b) stacked view for better visual observation.

As seen from Figure 6.7 (a,b), no prominent EPR vibration signal is observed for $CoO_x(OH)_y/C$, Co/Ce/C-1:1 and Co/Ce/C-9:1. This is an expected feature for a traditional heterogenite structure ($Co^{3+}OOH$) that it low spin and mostly diamagnetic [3]. On the other hand, there is a sharp and intense EPR signal for Co/Ce/C-3:1 at g =3.1 which indicates

the introduction of a large number of free electrons in Co/Ce/C-3:1 compared to Co/Ce/C-1:1 and Co/Ce/C-9:1. The more intense signals result from the unpaired electrons present at the oxygen vacancy sites and structural distortions [22–25]. This optimized d-orbital configuration of Co^{3+} ions in Co/Ce/C-3:1 which is brought about by an optimal ratio of Co:Ce could effectively enhance electrochemical properties of the $CoO_x(OH)_y/C$ moiety in it. Also, Co/Ce/C-3:1 exhibits a narrow EPR signals depicting lower degree of splitting. The hyperfine splitting is more prominent in the case of the other catalysts. This also puts light on the fact that Co-sites in Co/Ce/C-3:1 are in a different chemical environment than the other catalysts.

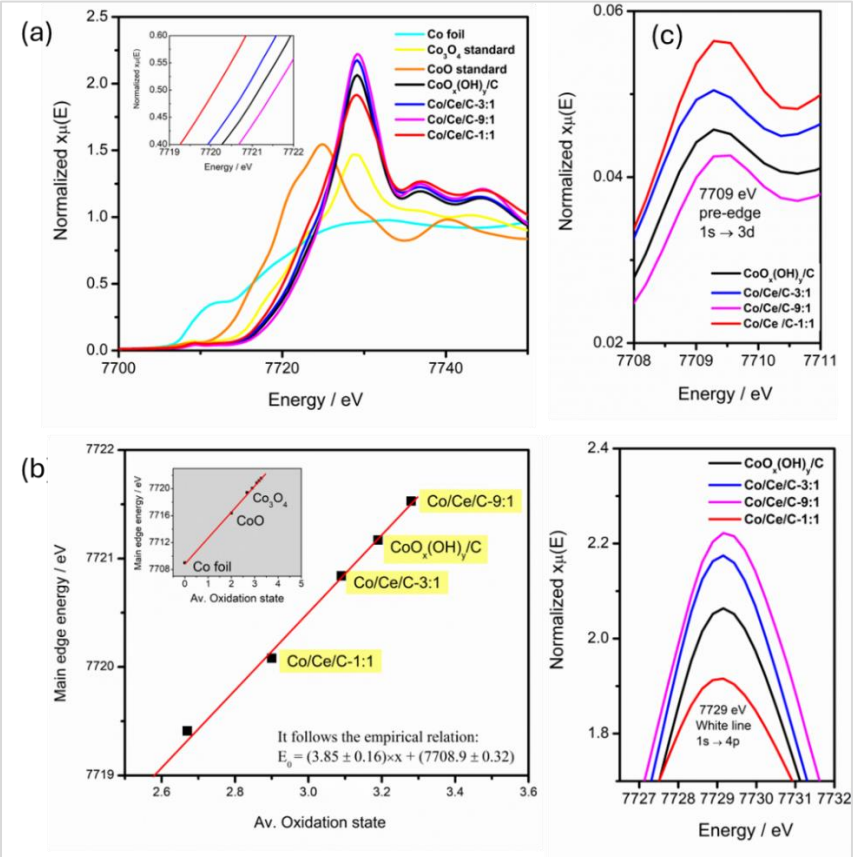

Figure 6.8. XANES spectra of the as-synthesized catalysts $CoO_x(OH)_y/C$, the Co/Ce/C hybrids, and three standards− Co foil, CoO, Co_3O_4.

XANES measurements are utilized to conduct a more in-depth investigation on average oxidation states and ligand symmetry in the as-synthesized materials. The XANES spectra and the derived average oxidation states are presented in Figure 6.8. Energy shifts of the absorption edge in XANES are directly related to the average oxidation state of the

adsorbent atom [25]. Inset of Figure 6.8 (a) highlights the absorption energy position at 0.5 (half-height) of the normalized XANES spectra. As seen from Figure 6.8 (b), the average oxidation state of cobalt in the as-prepared materials range from ~2.9 to 3.3. The Co/Ce/C-3:1 hybrid has a slightly lower average oxidation state compared to $CoO_x(OH)_y/C$. This could be presumed to occur under influence of CeO_2. Figure 6.8 (c) shows that a pre-edge feature at ~7,710 eV. Pre-edge is representative of 1s→3d transition. And the intensity of the pre-edge peak is correlated to the centrosymmetry of the octahedron [3]. This indicates that there is lower centrosymmetry in Co/Ce/C-3:1 hybrid than in $CoO_x(OH)_y/C$ which further confirms the presence of high-spin state Co^{3+}. Figure 6.8 (d) shows the white line region. White line is representative of 1s→4p transition. It is seen that white line of $CoO_x(OH)_y/C$ is broader and lower intensity than that of Co/Ce/C-3:1. A broader white line with lower intensity is representative of more splitting of 4p orbitals [3]. Hence, 4p orbitals are non-degenerate in $CoO_x(OH)_y/C$ which indicates that Co^{3+} is most likely to be present in low spin in Co/Ce/C- 3:1 and high spin in $CoO_x(OH)_y/C$.

6.1.2 Electrocatalytic study

The catalysts are subjected to electrochemical analysis in a 3-electrode experimental setup. All-important electrochemical benchmarks are tabulated in Table 6.4. Figure 6.9 shows the CV curves exhibited under N_2- and O_2-saturated 0.1M KOH. This shows that all the catalysts are responsive towards ORR. The LSVs of the catalysts were recorded at rotation rates 400, 900, 1600, 2500 and 3600 rpm. These voltammograms are shown in Figure 6.10. $Co_x(OH)_y/C$ exhibits flat plateau in the mass-transport region while CeO_2/C and the CeO_2-base hybrids exhibited skewed baseline beyond 0.5 V. Hence, all important ORR parameters have been considered till 0.5 V.

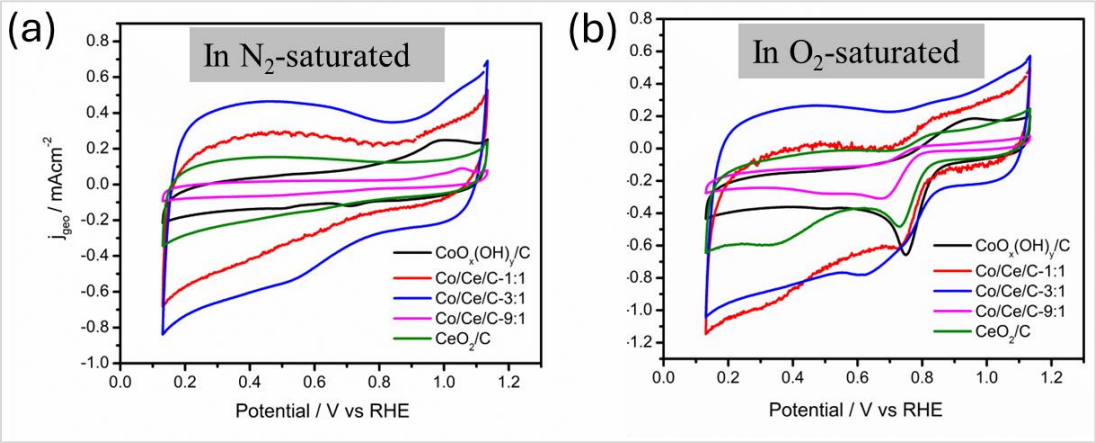

Figure 6.9. CVs of the catalysts in (a) N_2-saturated and (b) O_2-saturated 0.1M KOH at scan rate 10 mV s^{-1}.

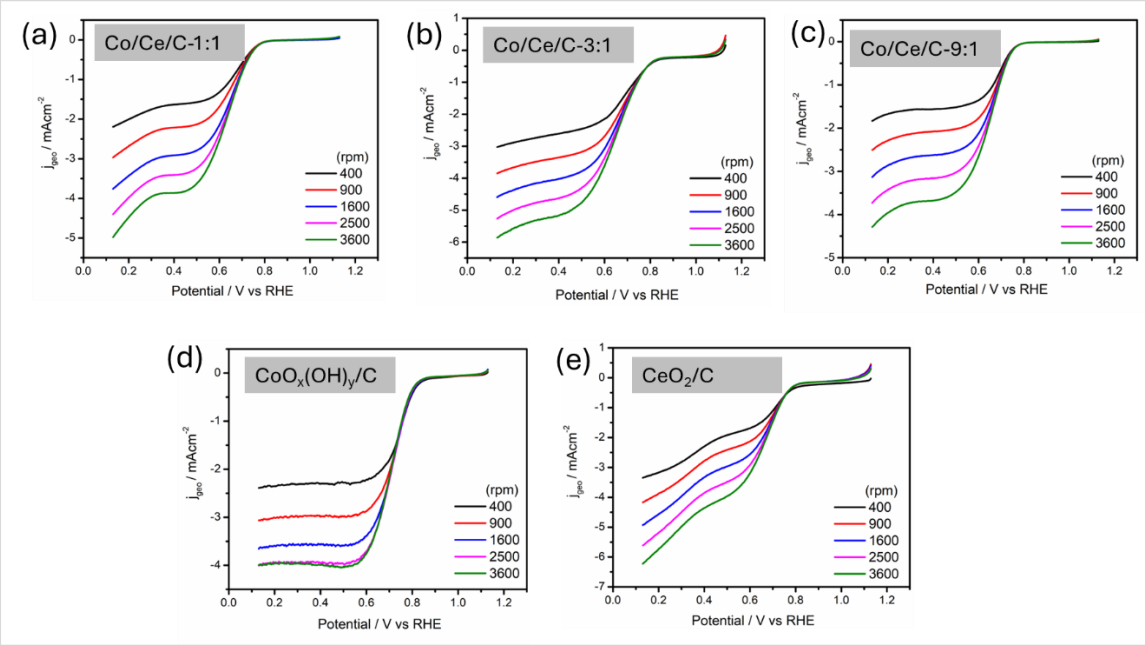

Figure 6.10. LSVs of the catalysts at different rotation rates from 400−3600 rpm for the Co/Ce/C hybrids (a) Co/Ce/C-1:1, (b) Co/Ce/C-3:1, (c) Co/Ce/C-9:1, (d) $CoO_x(OH)_y/C$, and (e) CeO_2/C.

The LSVs at 1600 rpm of all the catalysts under study are presented in Figure 6.11 (a) and the mass-transport limited current density at 0.5 V (j_{geo}@0.5V) are marked for comparison. The calculated mass-specific activities derived from this is presented in a bar diagram Figure 6.11 (b). It is observed that among the hybrids, Co/Ce/C-3:1 exhibits the

earliest onset for ORR ($E_{onset,ORR}$) and has the most positive half-wave potential ($E_{1/2}$). To compare the generated currents, the current densities at 0.5V is considered to avoid erroneous interpretation from additional reactions occurring beyond 0.5 V. This is assumed from the observation of a non-ideal pseudo-plateau region consisting of skewed baseline beyond 0.5 V.

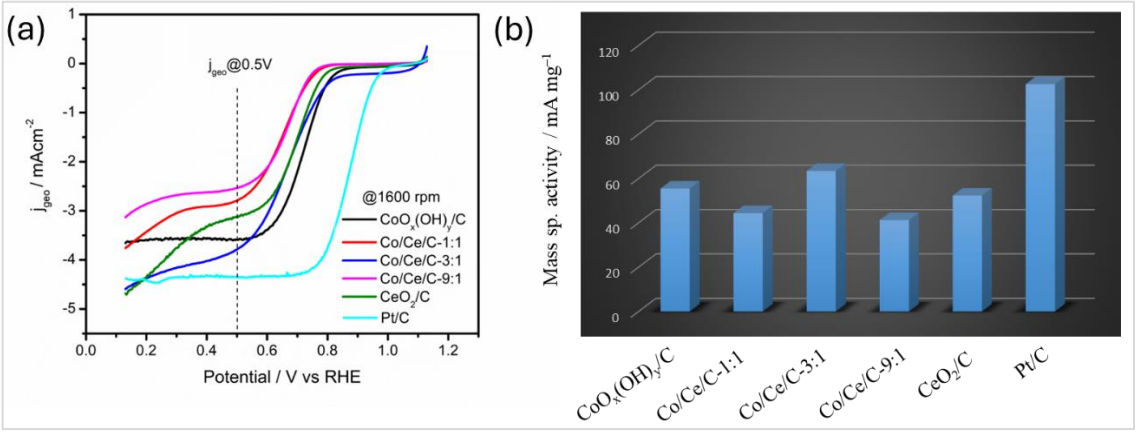

Figure 6.11. (a) LSVs of the catalysts and commercial Pt/C at 1600 rpm, and (b) bar diagram representing mass specific activities at 0.5V.

Figure 6.12 shows the CVs of the materials at different scan rates recorded to determine the ECSA. The double layer capacitance (C_{DL}) derived from the slope of current vs. scan rate plot and the derived mass-specific ECSAs for catalysts are presented in Figure 6.13. The numerical values of mass-specific ECSAs are presented in Table 6.4. This indicates that the Co/Ce/C-3:1has the maximum number of accessible active sites for ORR in the studied reaction conditions.

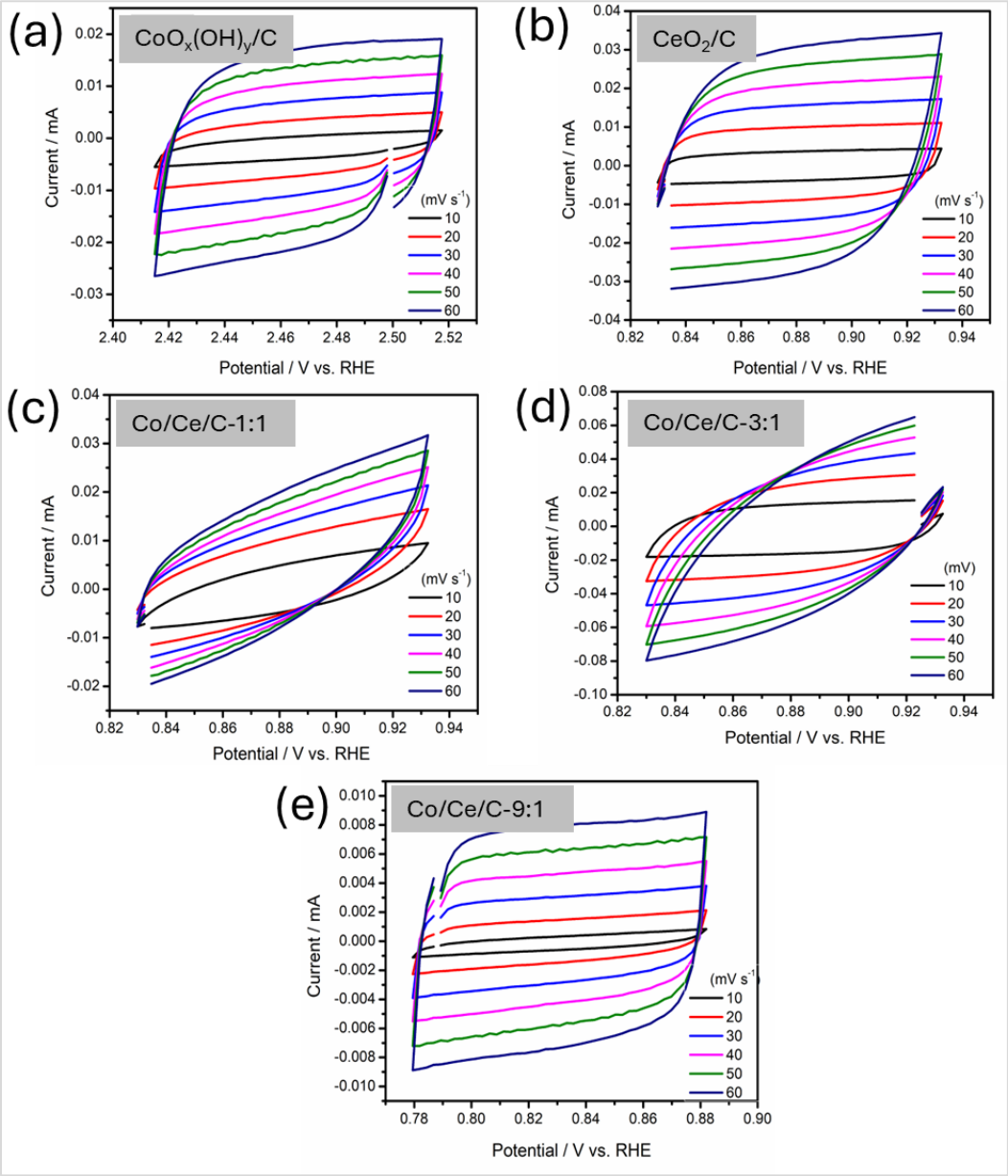

Figure 6.12. Scan rate dependent CVs of (a) $CoO_x(OH)_y/C$, (b) CeO_2/C, (c) Co/Ce/C-1:1 (d) Co/Ce/C-3:1, and (e) Co/Ce/C-9:1.

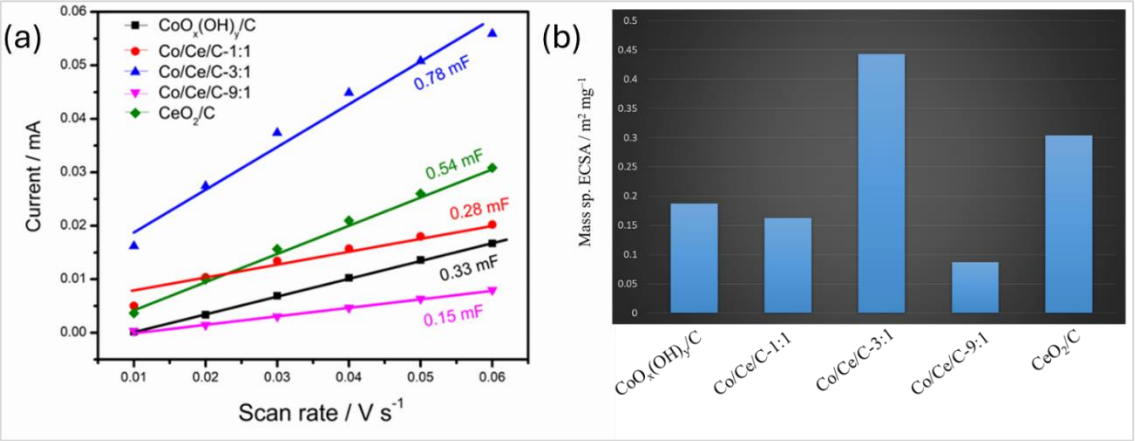

Figure 6.13. (a) Current vs. Scan rate plots with slope C_{DL}, and (b) bar diagram representing mass specific ECSA of the catalysts.

To get an insight into the kinetics of the electrocatalysts, Koutecky-Levich (K-L) plots are derived from their rotational LSVs as. It describes the generated current densities as a function of the angular momentum of the RDE. The equation is described in Section 2.6.6. The analysis is carried out in the potential window 0.55−0.7 V which falls in the mixed kinetic-diffusion region. The K-L plots are shown in Figure 6.14.

The lines exhibit good linearity and parallelism indicating that K-L assumptions hold good in the chosen window. The number of electrons transferred (n) was derived from '*B*'. This is represented by a bar diagram in Figure 1.4. It shows that 'n' for the Co/Ce/C-3:1 is the nearest to the ideal value (n_{ideal} =4) which is reported for the commercial benchmark catalyst 20 wt% Pt/C. The other hybrids Co/Ce/C-1:1 and Co/Ce/C-9:1 along with $CoO_x(OH)_y/C$ and CeO_2/C are far from 4. $CoO_x(OH)_y/C$ has n>>4 which indicates additional reactants possibility of unwanted reactants being reduced in addition to ORR.

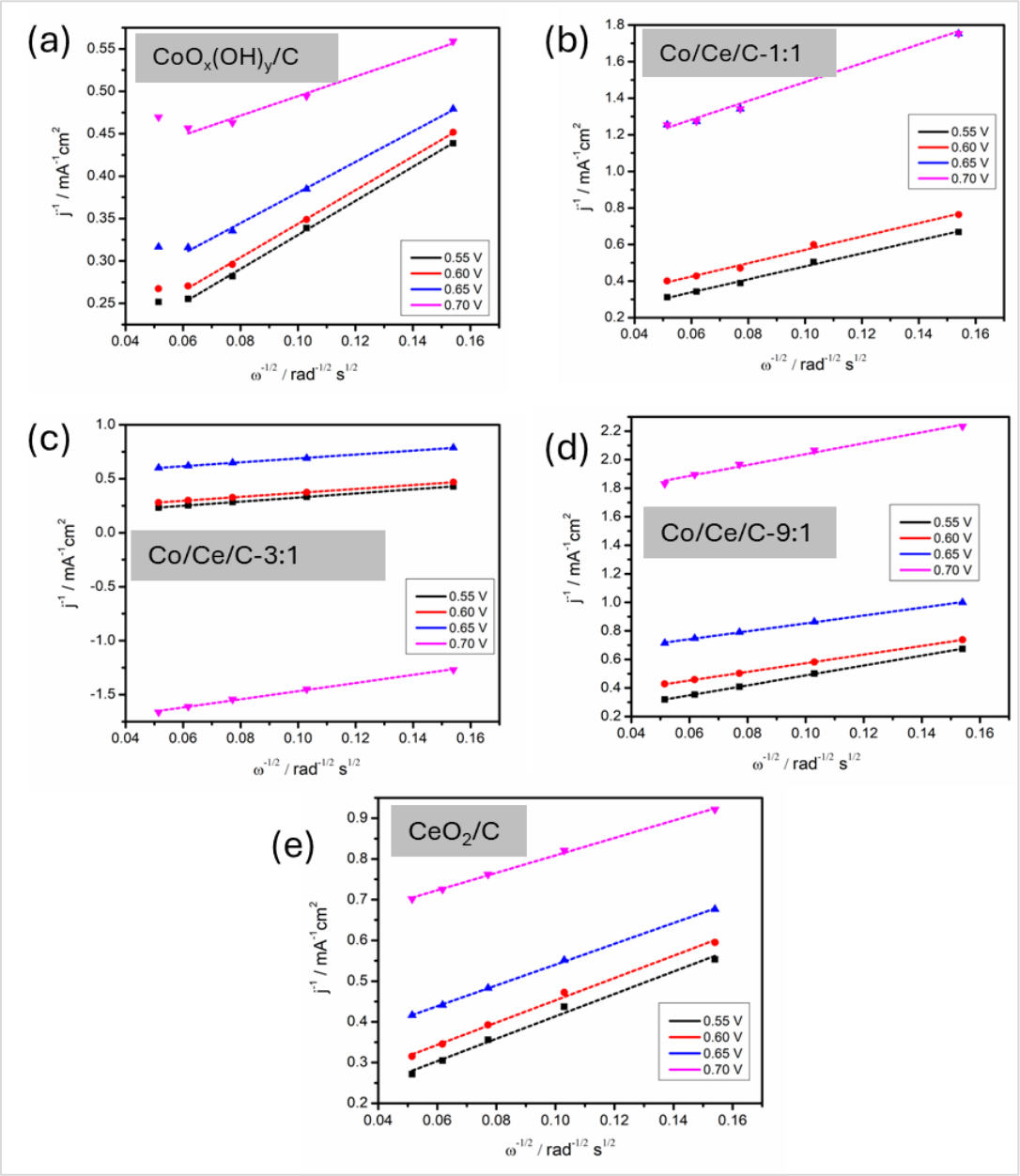

Figure 6.14. Koutecky-Levich (K-L) plots of (a) $CoO_x(OH)_y/C$, (b) Co/Ce/C-1:1, (c) Co/Ce/C-3:1, (d) Co/Ce/C-9:1, and (e) CeO_2/C.

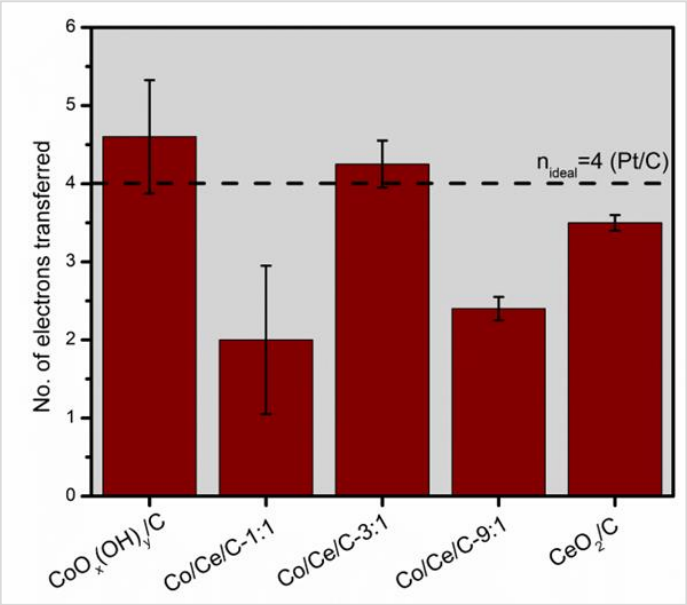

Figure 6.15. Average number of electrons transferred in potential range 0.55−0.7 V.

The catalysts were tested for stability and durability through ADT and CA tests. For ADT, the catalysts were subjected to 10,000 cycles of stationary CV. Its LSVs at rotation rate 1600 rpm, before and after 10,000 potential cycles were compared to note the shift in their half-wave potentials ($E_{1/2}$). This shift gives an estimate measure of its stability to withstand stress. The ADT test for the as-synthesized catalysts is shown in Figure 6.16. The shift in $E_{1/2}$ for the as-synthesized catalysts after ADT test of 10,000 cycles is compared to that of commercial benchmark catalyst 20 wt% Pt/C. This comparison is presented in a bar diagram in Figure 6.17 which shows that the hybrid Co/Ce/C-3:1 has a very minimal shift (~4 mV) compared to that exhibited by Pt/C (~28 mV). It also exhibits the least shift compared to $CoO_x(OH)_y/C$ and the other two hybrids Co/Ce/C-1:1 and Co/Ce/C-9:1. This puts stress on the fact that a 3:1 atomic ratio of Co/Ce is optimal for enhanced stability during catalysis of ORR.

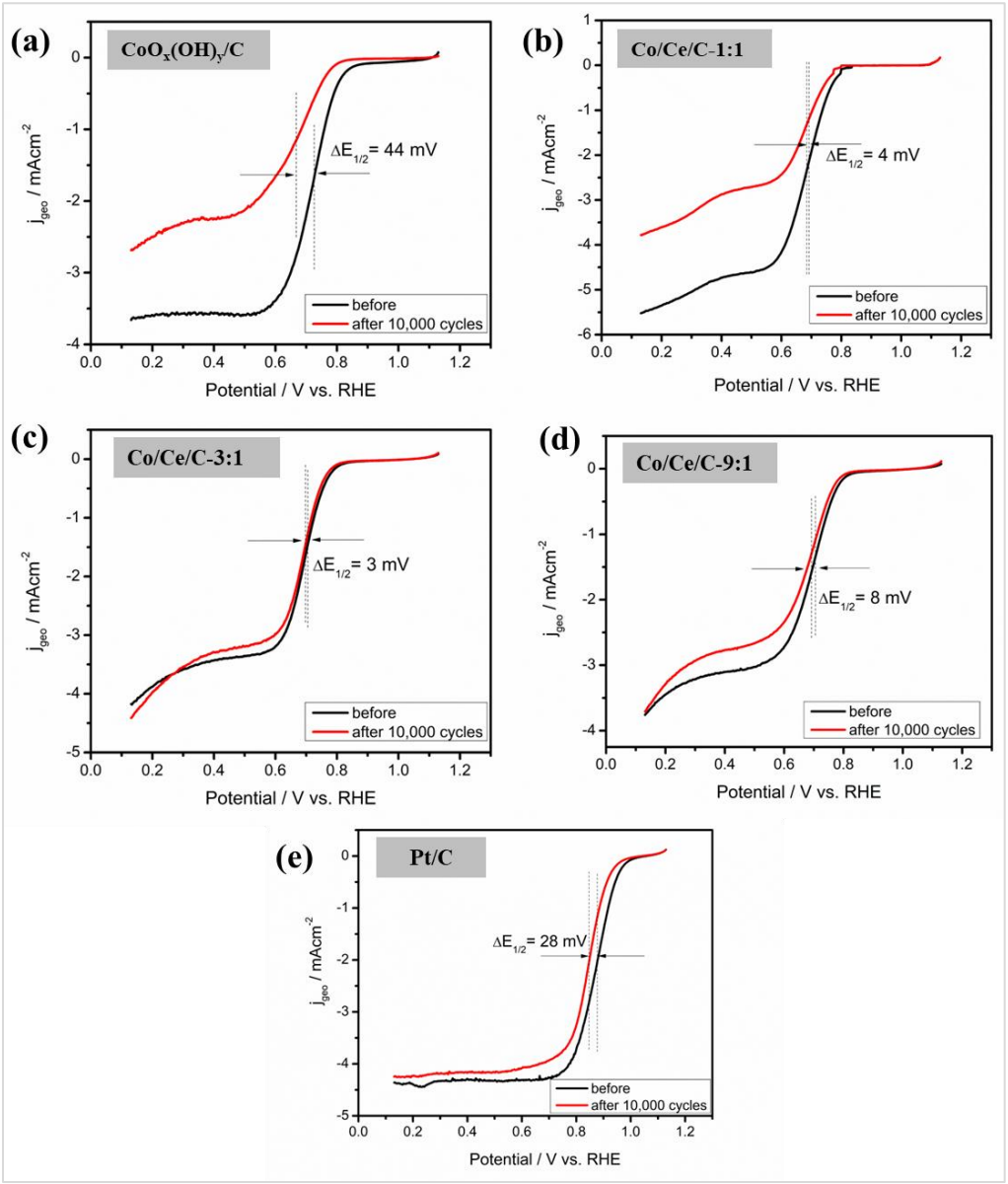

Figure 6.16. LSVs of the as-synthesized catalysts (a) $CoO_x(OH)_y/C$, (b) Co/Ce/C-1:1, (c) Co/Ce/C-3:1, (d) Co/Ce/C-9:1, and (e) commercial 20 wt.% Pt/C before and after 10,000 CVs.

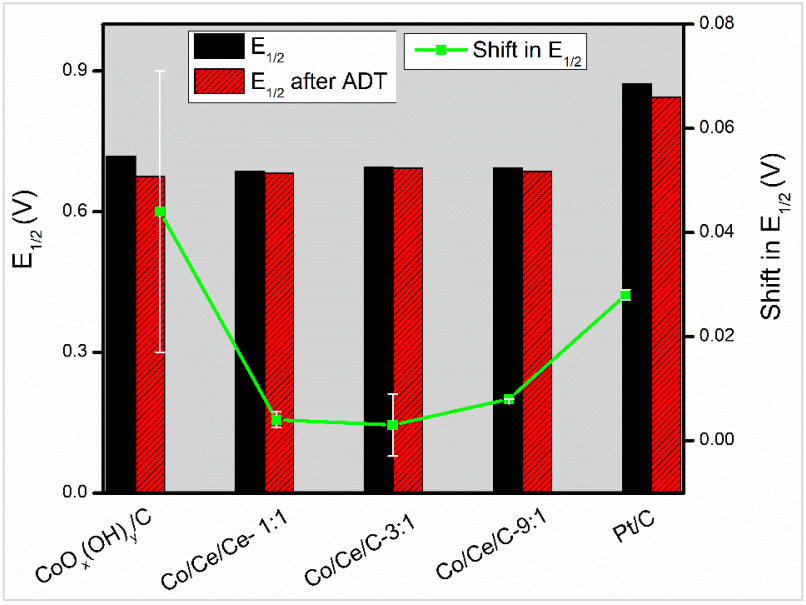

Figure 6.17. Bar diagram consisting of half-wave potentials ($E_{1/2}$) before and after ADT test and the corresponding shifts in $E_{1/2}$ are shown by line diagram.

This hybrid Co/Ce/C-3:1 was subjected to a 5.5 h long CA test under rotating condition at 1600 rpm and compared with 20 wt% Pt/C. The potential was held at 0.5 V. The results are shown in Figure 6.18. shows the decrease in generated currents with passing time is shown in Figure 6.18 (a) and the % retention of their initial currents at the end of the CA test is presented in a bar diagram in Figure 6.18 (b). These results clearly indicate that the hybrid Co/Ce/C-3:1 is more durable than the commercial standard for ORR.

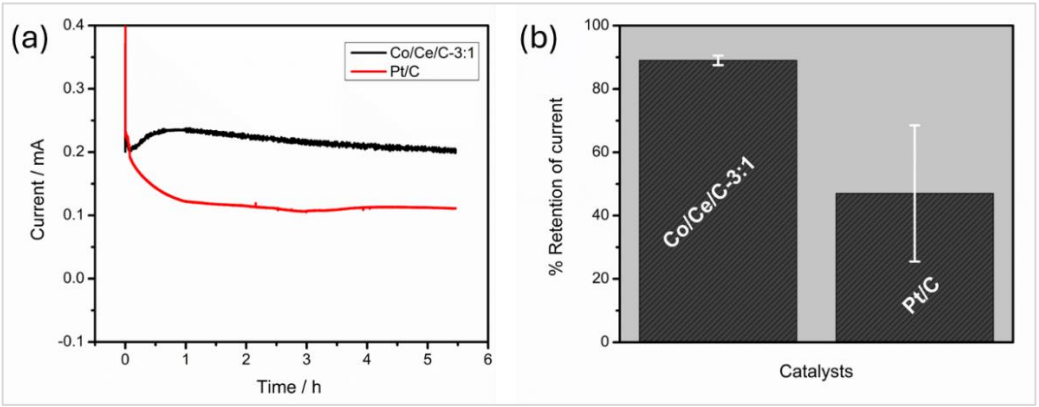

Figure 6.18. (a) Chronoamprometry (CA) test results of $CoO_x(OH)_y/CeO_2$ 3:1 and commercial 20 wt% Pt/C conducted at 0.4 V, and (b) Bar diagram representing the % current retention of CA test.

The catalysts were also tested for OER in the same reaction conditions. This time the electrolyte is not saturated with N_2 only. The LSVs@1600 rpm for OER are presented in Figure 6.19 (a). This shows that the Co/Ce/C hybrids have a faster kinetics for OER compared to the $CoO_x(OH)_y/C$ and CeO_2/C. This statement is made from the observation that the Co/Ce/C hybrids reach 10 mA cm^{-2} (j_{10}) earlier than $CoO_x(OH)_y/C$ and CeO_2/C. This time the hybrid with Co/Ce/C-1:1 has the earliest j_{10}. Hence, the Co/Ce/C hybrids could be referred to as bifunctional catalysts for ORR and OER. The overpotentials are calculated employing the equation $\eta\ /V = E(j10) - 1.23$ as described in Section 2.6.10 and the results are presented in a bar diagram in Figure 6.19 (b). It is observed that the overpotentials are very high compared to that of the benchmark catalyst for OER i.e. RuO_2.

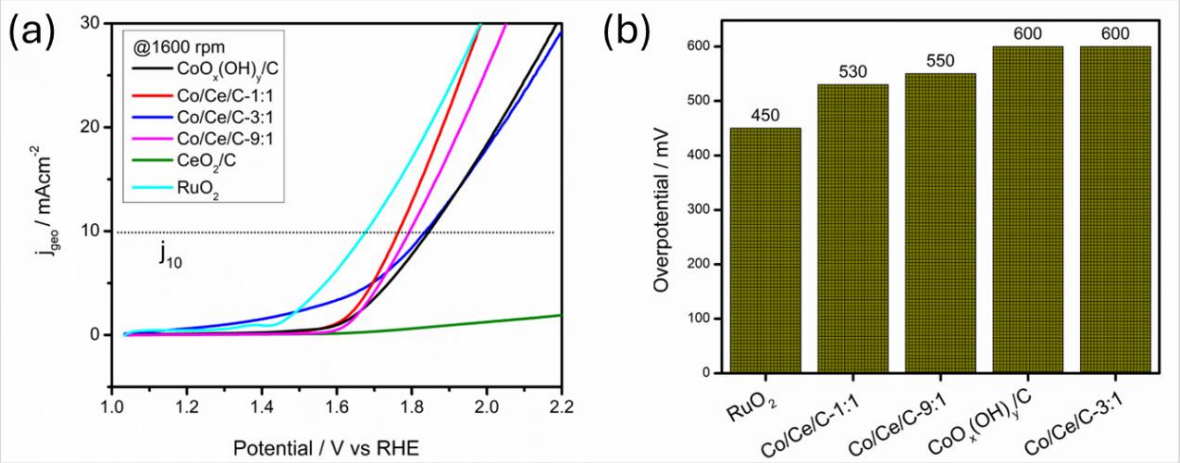

Figure 6.19. (a) RDE-LSVs of the as-synthesized catalysts at 1600 rpm for OER in N_2-saturated 0.1M KOH and scan rate 10 mV s^{-1}. The dotted line represents the current density of 10 mA cm^{-2}. (b) Bar diagram representing the overpotentials.

Table 6.4. Summary of $E_{onset,ORR}$, Ej10, η and Tafel slopes of various ECs and RuO_2 for OER derived from LSV curve at 1600 rpm.

Catalysts	$E_{onset,ORR}$ / V	Sp. ECSA / $m^2\ mg^{-1}$	Sp. Activity @0.5V / $mA\ mg^{-1}$	$E_{1/2}$ / V	Ej10 / V	η / mv
$CoO_x(OH)_y/C$	0.87	0.186	55.46	0.72	1.84	600
Co/Ce/C-1:1	0.82	0.162	44.37	0.65	1.76	530
Co/Ce/C-3:1	0.85	0.442	63.38	0.68	1.83	600
Co/Ce/C-9:1	0.80	0.086	41.20	0.66	1.79	550
CeO_2/C	0.84	0.30	52.29	0.68	Did not attain j10	–
Pt/C	1.00	–	102.56	0.87	–	–
RuO_2	–	–	–	–	1.67	450

From the above discussion, we can comprehend that cobalt to cerium atomic ratio plays a vital role in the physicochemical properties in the $CoO_x(OH)_y/CeO_2/C$ catalysts. It alters the Co^{2+} : Co^{3+} ratios in the Co/Ce/C hybrids. This occurs concurrently with similar changes in Ce^{3+} : Ce^{4+} ratios (as seen in Table 6.2 and Table 6.3) which simultaneously affects the average oxidation state of the active cobalt sites in the catalysts. The hybrid Co/Ce/C-3:1 has the greatest number of point defects. This factor could be attributed to its enhanced electrochemical performance towards ORR. Furthermore, the varying Co/Ce ratio affects the stability of the catalysts. The 3:1 exhibits the least shift in $E_{1/2}$ and the highest retention of current in the stability tests. Similarly, Co/Ce/C-1:1 with a lesser paramagnetism (g=2.2) exhibits the earliest onset for OER. One important point observed is that both 1:1 and 3:1 are paramagnetic while $CoO_x(OH)_y/C$ and Co/Ce/C-9:1 are nearly diamagnetic. Hence, we can assume that a high spin Co3+ is beneficial for both ORR and OER.

6.2 Conclusions

In summary, we have synthesized $CoO_x(OH)_y/CeO_2$ nanohybrids with varying degrees of Co/Ce atomic ratios via simple hydrothermal approach, followed by carbonization with graphene nanoplatelets. The electrocatalytic activities of the resultant

materials were evaluated by CV and RDE-LSV techniques. All catalysts were bifunctional toward ORR and OER. For ORR, the Co/Ce/C-3:1 delivers an improved $E_{onset,ORR}$, a high specific activity, higher specific ECSA, proceeds via favorable $4e^-$ reduction pathway, accompanied by high stability and high durability compared to that of commercial 20 wt.% Pt/C. For OER, on the other hand, Co/Ce/C-1:1 displays earliest Ej10 and least overpotential among the as-synthesized catalysts. However, the OER overpotentials of the synthesized hybrids are not very impressive in comparison to the commercial benchmark RuO_2. Nonetheless, the study puts light on the importance of intricate tuning of oxide/hydroxide interfaces by optimal Co/Ce ratios that eventually enhance electrocatalytic ability.

References

[1] Jia, H., Yao, N., Yu, C., and Cong, Hengjiang and Luo, W. unveiling the electrolyte cations dependent kinetics on CoOOH-catalyzed oxygen evolution. *Angewandte Chemie - International Edition*, 62(49):1−8, 2023.

[2] Zhang, S., Yu, T., Wen, H., and Ni, Z. The latest development of CoOOH two-dimensional materials used as OER catalysts. *ChemComm*, 56:15387−15405, 2020.

[3] Zhang, X., Zhong, H., Zhang, Q., Zhang, Q., Wu, C., Yu, J., Ma, Y., An, H., Wang, H., Zou, Y., Diao, C., Chen, J., Yu, Z. G., Xi, S., Wang, X., and Xue, J. High-spin Co^{3+} in cobalt oxyhydroxide for efficient water oxidation. *Nature Communications*, 15(1):1−10, 2024.

[4] Zhang, B., Shan, J., Wang, W., Tsiakaras, P., and Li, Y. Oxygen vacancy and core–shell heterojunction engineering of anemone-like CoP@CoOOH bifunctional electrocatalyst for efficient overall water splitting. *Small*, 18(12):1−13, 2022.

[5] Shi, L., Fan, C., Fu, X., Yu, S., Qian, G., and Wang, Z. Carbonate-assisted hydrothermal synthesis of porous hierarchical Co_3O_4/CuO composites as high capacity anodes for lithium-ion batteries. *Electrochimica Acta*, 197:23−31, 2016.

[6] Feng, Z., Bao, W., Xu, X., Ma, X., Zhan, J., and Yin, Y. Heteroepitaxial growth of well-dispersed Co_3O_4 nanocatalysts on porous ZnO nanoplates via successive hydrothermal deposition. *ChemNanoMat*, 2(10):946−951, 2016.

[7] Chenari, H. M., Riasvand, L., and Khalili, S. The synthesis condition and

characterization of thermally treated CeO_2 and ZnO-CeO_2 composite fibers. *Ceramics International*, 45(11):14223−14228, 2019.

[8] Afzal, S., Quan, X., and Lu, S. Catalytic performance and an insight into the mechanism of CeO_2 nanocrystals with different exposed facets in catalytic ozonation of p-nitrophenol. *Applied Catalysis B: Environmental*, 248:526−537, 2019.

[9] Goswami, C., Hazarika, K. K., Yamada, Y., and Bharali, P. Nonprecious hybrid metal oxide for bifunctional oxygen electrodes: endorsing the role of interfaces in electrocatalytic enhancement. *Energy & Fuels*, 35(16):13370−13381, 2021.

[10] Naebe, M., Wang, J., Amini, A., Khayyam, H., Hameed, N., Li, L. H., Chen, Y., and Fox, B. Mechanical property and structure of covalent functionalised graphene/epoxy nanocomposites. *Scientific Reports*, 4:1−7, 2014.

[11] Smyrnioti, M., and Ioannides, T. Synthesis of cobalt-based nanomaterials from organic precursors. In. Maaz, K., editor, *Cobalt*, pages 49–69, ISBN:978-953-51-3667-5. IntechOpen, Croatia, 2017.

[12] Liu, Y. C., Koza, J. A., and Switzer, J. A. Conversion of electrodeposited $Co(OH)_2$ to CoOOH and Co_3O_4, and comparison of their catalytic activity for the oxygen evolution reaction. *Electrochimica Acta*, 140:359−365, 2014.

[13] Sanpo, N., Siao, A., Ang, M., Hasan, F., Wang, J., and Berndt, C. C. Phases and microstructures of solution precursor plasma sprayed cobalt ferrite splats. In *Asian Thermal Spray Conference* (ATSC2012), volume 5, pages 145−146, Tsukuba, Japan, 2012.

[14] Polychronopoulou, K., Alkhoori, A. A., Efstathiou, A. M., Jaoude, M. A., Damaskinos, C. M., Baker, M. A., Almutawa, A., Anjum, D. H., Vasiliades, M. A., Belabbes, A., Vega, L. F., Zedan, A. F., and Hinder, S. J. Design aspects of doped CeO_2 for low-temperature catalytic CO oxidation: transient kinetics and DFT approach. *ACS Applied Materials and Interfaces*, 13(19):22391−22415, 2021.

[15] Johra, F. T., Lee, J. W., and Jung, W. G. Facile and safe graphene preparation on solution based platform. *Journal of Industrial and Engineering Chemistry*, 20(5):2883−2887, 2014.

[16] Malard, L. M., Pimenta, M. A., Dresselhaus, G., and Dresselhaus, M. S. Raman spectroscopy in graphene. *Physics Reports*, 473(5-6):51-87, 2009.

[17] Liu, S., Tan, X., Zheng, X., Liang, S., He, M., Liu, J., Luo, J., and Zhang, H. One-step microwave synthesis CoOOH/$Co(OH)_2$/CNT nanocomposite as superior electrode material for supercapacitors. *Ionics*, 26(7):3531−3542, 2020.

[18] Goswami, C., Borah, B. J., Das, R., Tada, K., Tanaka, S., Prosvirin, I. P., Ismagilov, I. Z., Matus, E. V., Kerzhentsev, M., and Bharali, P. CeO_2 promotes electrocatalytic formic acid oxidation of Pd-based alloys. *Journal of Alloys and Compounds*, 948:1−10, 2023.

[19] Liu, Y., Ma, C., Zhang, Q., Wang, W., Pan, P., Gu, L., Xu, D., Bao, J., and Dai, Z. 2D Electron gas and oxygen vacancy induced high oxygen evolution performances for advanced Co_3O_4/CeO_2 nanohybrids. *Advanced Materials*, 31(21):1-9, 2019.

[20] Kim, K. H., and Choi, Y. H. Surface oxidation of cobalt carbonate and oxide nanowires by electrocatalytic oxygen evolution reaction in alkaline solution. *Materials Research Express*, 9(3):1−11, 2022.

[21] Zhang, Z., Luo, L., Ding, X., Zhou, S., and Zeng, J. Regulating spin states in oxygen electrocatalysis. *Angewandte Chemie - International Edition*, 62(15): 1−13, 2023.

[22] Karmakar, A., Karthick, K., Sankar, S. S., Kumaravel, S., Ragunath, M., and Kundu, S. Oxygen vacancy enriched $NiMoO_4$ nanorods via microwave heating: a promising highly stable electrocatalyst for total water splitting. *Journal of Materials Chemistry A*, 9(19):11691−11704, 2021.

[23] Liu, J., Lu, Y., and Jian, P. Direct Synthesis of α - Methoxyphenylacetic acid via tandem catalysis from styrene and methanol with $Co_3O_4/CuCo_2O_4$ heterostructures. *Catalysis Letters*, 153(11):3504−3515, 2023.

[24] Arun Karmakar, Kannimuthu Karthick, Sangeetha Kumaravel, Selvasundarasekar Sam Sankar, and S. K. Enabling and inducing oxygen vacancies in cobalt iron layer double hydroxide via selenization as precatalysts for electrocatalytic hydrogen and oxygen evolution reactions. *Inorganic Chemistry.*, 60:2023−2036, 2023.

[25] Huang, Y., Zhao, X., Tang, F., Zheng, X., Cheng, W., Che, W., Hu, F., Jiang, Y., Liu, Q., and Wei, S. Strongly electrophilic heteroatoms confined in atomic CoOOH

nanosheets realizing efficient electrocatalytic water oxidation. *Journal of Materials Chemistry A*, 6:3202−3210, 2018.